



CO2 plume and pressure monitoring through pressure sensors above the caprock

Xiaojin Zheng, D. Nicolas Espinoza, Matthieu Vandamme, Jean-Michel Pereira

► To cite this version:

Xiaojin Zheng, D. Nicolas Espinoza, Matthieu Vandamme, Jean-Michel Pereira. CO2 plume and pressure monitoring through pressure sensors above the caprock. International Journal of Greenhouse Gas Control, 2022, 117, 39 p. <10.1016/j.ijggc.2022.103660>. <hal-03905395>

HAL Id: hal-03905395

<https://enpc.hal.science/hal-03905395v1>

Submitted on 18 Dec 2022

HAL is a multi-disciplinary open access archive for the deposit and dissemination of scientific research documents, whether they are published or not. The documents may come from teaching and research institutions in France or abroad, or from public or private research centers.

L'archive ouverte pluridisciplinaire **HAL**, est destinée au dépôt et à la diffusion de documents scientifiques de niveau recherche, publiés ou non, émanant des établissements d'enseignement et de recherche français ou étrangers, des laboratoires publics ou privés.



Distributed under a Creative Commons CC BY 4.0 - Attribution - International License

CO₂ Plume and Pressure Monitoring through Pressure Sensors above the Caprock

Xiaojin Zheng, D. Nicolas Espinoza

*Hildebrand Department of Petroleum and Geosystems Engineering, The University of Texas at Austin,
Texas, USA*

Matthieu Vandamme, Jean-Michel Pereira

Navier, École des Ponts, Université Gustave Eiffel, CNRS, Marne-la-Vallée, France

Abstract

Commercial-scale development of CO₂ geological storage necessitates robust and real-time monitoring methods to track the injected CO₂ plume and provide assurance of CO₂ storage. Pressure monitoring above the injection zone is a method to detect potential CO₂ leaks into overlying formations. We present a generic CO₂ storage model with a single injector to predict pressure changes above the caprock due to both fast hydraulic communication and partially undrained loading, the latter often neglected in reservoir simulation. The simulation used a compositional simulator coupled with geomechanics to solve the poroelastic equations in the entire storage complex. The results show that changes of pore pressure above the caprock caused by partially undrained loading reach up to ~15 kPa within ~10 days followed by a gradual decay with time. This is about 1% of the pressure increase in the injection zone. Furthermore, the pressure changes above the caprock are closely related to the advance of the CO₂ plume. The results also include forward simulations considering the presence of: a fault either with high or low permeability, a poorly isolated abandoned well, a leaky injector, and a second injector. Fluid flow through high permeability paths across the caprock favors a ~one order of magnitude higher, yet more gradual pressure increase than the base case with a fully covering caprock. Pressure monitoring above the caprock is a feasible technology to

track the CO₂ plume, requires high precision pressure measurements, and must account for partially undrained poroelastic loading to interpret correctly measured pressure signals in the field.

Keywords: poroelasticity, CCUS, wellbore instrumentation, leaks, caprock integrity

1. Introduction

The successful development of carbon dioxide (CO₂) geological storage necessitates robust and real-time monitoring methods to detect potential CO₂ leakage into overlying formations and provide assurance for permanent CO₂ trapping (Kim & Hosseini, 2015; Meckel et al., 2008). Most monitoring techniques are based on measurements on the surface and in the injection zone. On-surface monitoring (such as 4D seismic and InSAR mapping) can capture large geophysical features but is limited by high costs, laborious interpretation, difficulty to capture low CO₂ saturations, and a large attenuation of signals imposed by the overburden (Arts et al., 2004; Rutqvist et al., 2010). Monitoring in the injection zone (IZ) involves fluid sampling, rock analysis, and placement of sensors in the target formation, enables direct access to the zone of interest, and offers direct evidence for leak detection, but remains limited to a few observation wells and small sampling volumes (Ajo-Franklin et al., 2013; Hovorka et al., 2006; Zeidouni & Pooladi-Darvish, 2012b, 2012a).

Pressure monitoring above the injection zone (AIZ) is an alternative approach to monitor CO₂ injection and detect undesirable migration of fluids from the injection zone to overlying formations (Liebscher et al., 2013; Park et al., 2012; Wiese et al., 2013; Zhang et al., 2019). AIZ pressure monitoring can be done above the injection point but in the same storage formation, e.g. Decatur and Otway field cases (Bauer et al., 2016; Ennis-King et al., 2017), or above the caprock, e.g. Cranfield and Ketzin field cases (S. Hosseini et al., 2018; Wiese et al., 2013). AIZ pressure monitoring is relatively inexpensive, covers a wider area than the IZ monitoring, and has the potential to detect leaks into overlying formations if monitored above the caprock (S. Hosseini et al., 2018). This type of monitoring takes advantage of the pressure changes caused by injection with a pressure front moving

faster than the injected fluid (Rutqvist 2012). Significant work has been done to predict and identify leakages through abandoned wellbores due to direct hydraulic communication between the IZ and the AIZ through analytical models and numerical simulation (Cihan et al., 2013; González-Nicolás et al., 2015; Jung et al., 2013; Namhata et al., 2016; Sun & Durlofsky, 2019; Zhang et al., 2018).

Pore pressure increases above the caprock were thought to be zero in the absence of high permeability paths across the caprock or adjacent faults with high permeability. Thus, any deviation from the pressure baseline (expected to be constant) was considered as a result of high hydraulic communication that could become a potential leak if the high permeability path is reached by the CO₂ plume. However, recent pressure monitoring in the Cranfield CO₂ injection project indicates measurable changes of pore pressure above the caprock (~50 kPa) after two years of CO₂ injection with IZ pressure change reaching a maximum of ~8.8 MPa in the absence of leaks (Kim & Hosseini, 2014; Tao et al., 2012). Analytical and numerical simulation work demonstrates that rock deformation above the injection zone can induce pressure changes in the absence of leaks through the caprock, by means of a poroelastic phenomenon known as “undrained loading” (Kim & Hosseini, 2014; Zeidouni & Vilarrasa, 2016). Despite recent advances and numerical simulations, pressure monitoring above the caprock remains largely underutilized or misinterpreted because of a lack of (1) validation schemes, (2) discrimination between fast hydraulic communication and undrained loading, (3) thorough measurement of poromechanical properties of the AIZ, (4) thorough deployment of high-resolution sensors to capture subtle pressure changes (e.g., 1 kPa), (5) coupled poroelastic simulation beyond the injection zone for all CO₂ storage projects, (6) extension of existing models to two-phase fluid flow, (7) accurate prediction of absolute magnitude and transient pressure changes in the AIZ, and (8) evaluation of other leaking/sealing scenarios beyond just one leaky abandoned well (S. Hosseini et al., 2018; S. A. Hosseini, 2019; S. Hosseini & Alfi, 2016; Kim & Hosseini, 2014; Mishra et al., 2014; Wiese et al., 2013; Zeidouni & Vilarrasa, 2016).

CO₂ injection and reservoir pressurization cause displacements and deformations far beyond the extent of the CO₂ plume (Rutqvist et al., 2010; Segall & Fitzgerald, 1998; Tang et al., 2021). Fluid injection and reservoir pressurization may result in ground surface uplift due to expansion of the reservoir caused by decreased effective stress. For example, InSAR data showed a surface uplift on the order of 5 mm per year in the In Salah Gas Project in Algeria (with a CO₂ injection rate of 0.5–1 Mt/year) (Rutqvist et al., 2009, 2010). CO₂ injection and reservoir pressurization also causes rock deformation between the surface and the reservoir which may appear as a change of pore pressure in fluid-saturated rocks (Detournay & Cheng, 1988; Roussel & Agrawal, 2017; Segall & Fitzgerald, 1998; Zeidouni & Vilarrasa, 2016). During a drained process, the application of an external stress induces volumetric strains without change of pore pressure. In contrast, pore pressure will increase in an undrained process when a (contraction) volumetric deformation is applied to a fluid-filled porous material (Cheng, 2016; Coussy, 2004). Hence, even in the absence of fast hydraulic communication between the injection zone and formations above the caprock, CO₂ (or any fluid) injection can modify the pore pressure above the caprock due to undrained loading.

In general, two mechanisms can contribute to pore pressure changes in porous media (1) advective fluid transport and (2) pore volume deformation. These coupled pore pressure diffusion and mechanical deformation processes are captured by the pressure P diffusivity equation for fluid flow coupled with poroelasticity with respect to time t (Cheng, 2016; Coussy, 2004; Detournay & Cheng, 1993):

$$\frac{\partial P}{\partial t} = \frac{kM^*}{\mu} \nabla^2 P - \alpha M^* \frac{\partial \varepsilon_V}{\partial t} \quad (1)$$

where k is the porous medium permeability, μ is the fluid viscosity, α is the Biot coefficient, ε_V is the bulk volumetric strain, and the Biot modulus M^* is

$$M^* = \left(\frac{\phi_0}{K_f} + \frac{\alpha - \phi_0}{K_m} \right)^{-1} \quad (2)$$

where ϕ_0 is the initial rock porosity, K_f is the bulk modulus of the pore fluid, and K_m is the bulk modulus of the rock matrix. Notice that Eq. 1 is the pressure diffusivity equation with total compressibility ($C_t = 1/M^*$), where the second term in the right-hand side captures the impact of rock deformation on pressure changes. Reservoir simulation without geomechanical coupling (or just one-way coupling) captures the first term on the right-hand side of Eq. 1 only.

For a linear elastic isotropic porous solid, the expected pore pressure change ΔP under undrained loading (no change in fluid mass within pore volume) is directly proportional to the imposed volumetric strain (Coussy, 2004):

$$\Delta P = -\alpha M^* \Delta \varepsilon_V \quad (3)$$

Thus, pore pressure change due to undrained loading depends on rock poroelastic properties, fluid compressibility $(K_f)^{-1}$, and volumetric strain. Decreases in pore volume lead to increases of pore pressure, while increases in pore volume lead to decreases of pore pressure for fully or partially undrained loading (Fig. 1).

Whether a process is undrained or drained depends on the rate of (strain) loading and the rate of pore pressure diffusion. Perfect fluid containment is rare in natural environments, so most processes can be generalized as partially undrained depending on the time interval of analysis. For example, the characteristic time of pressure diffusion T_{ch} captures the time when $\sim 2/3$ of the pore pressure is dissipated from an initial undrained loading state (Cheng, 2016):

$$T_{ch} = \frac{L^2}{D_h} \quad (4)$$

where L is the characteristic drainage length and $D_h = \frac{kM^*}{\mu}$ is the hydraulic diffusivity. Higher permeability and shorter characteristic distance of drainage decrease the characteristic pore pressure diffusion time and the magnitude of pore pressure increase for partially undrained loading of real sediments (Fig. 1). Thus, the partially undrained condition entails a smaller amount of pore

pressure variations than the fully undrained condition due to pressure dissipation. In fact, if the rate of (strain) loading is lower than the rate of pore pressure diffusion, a porous medium may never experience a pore pressure change due to pore volume reduction. Additional constitutive equations for the multiphase fluid flow, the poroelastic solid, and coupled hydro-mechanical simulation are available elsewhere (Cheng, 2016; Coussy, 2004; Prevost, 2013; Tran et al., 2009).

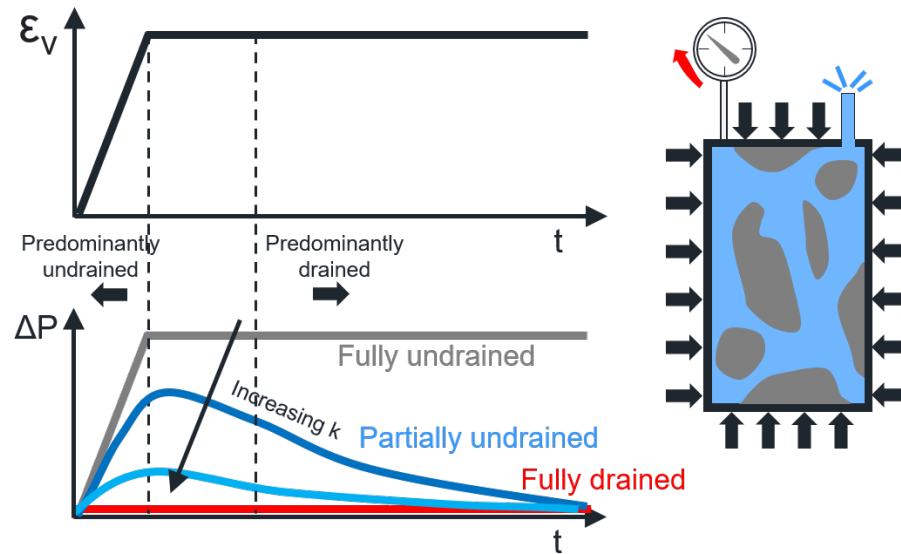


Fig. 1. Comparison among fully drained, partially undrained, and undrained conditions: the pore pressure changes under the partially undrained condition are proportional to the imposed volumetric strain but also depend on the hydraulic diffusivity of the porous medium.

The objective of this paper is to extend the current knowledge on pore-pressure monitoring above the caprock, mostly limited to leakages due to hydraulic communication, and make evident the impact of deformation-induced partially undrained loading. Such improvement is critical to establish pore-pressure monitoring above the caprock as a new subsurface signal that can potentially track the CO₂ plume, quantify hydraulic communication, detect possible leaks, and help ensure safe CO₂ storage. The paper starts with a description of the compositional fluid flow model coupled with geomechanics. We put special emphasis on examining the poroelastic response above the caprock by

analyzing the magnitude, evolution, and distribution of the pressure increase through forward modeling. The modeling work excludes pressure monitoring above the injection point but within the same storage formation, since such response is expected to be dominated by fluid advection. The analysis also discusses the possible configuration of pressure sensors regarding their position with respect to the injector, horizontally and vertically above the caprock. The discussion section considers the presence of various subsurface scenarios relevant to inverse analysis, including the presence of a poorly isolated injector wellbore, a leaky abandoned wellbore, a high-permeability/sealing fault, and two injectors.

2. Methodology

We use a fluid-flow compositional model coupled with poroelasticity for the entire storage complex, including overburden and underburden layers, which are usually ignored in reservoir simulation. All the materials are assumed to be mechanically and hydraulically isotropic. The model is handled through the reservoir simulator CMG-GEM; details about the model formulation, coupling scheme, and validation are available elsewhere (Computer Modeling Group Ltd., 2013; Ryu et al., 2019; Tran et al., 2009). The storage complex extends 12 km by 12 km in the lateral direction (49 blocks by 49 blocks) and 6 km in the vertical direction (48 blocks), totaling 115,248 grid blocks (Fig. 2). The grid size is gradually reduced from the reservoir boundary to the center of the injection point. The grid size ($dx \times dy \times dz$) near the injector is 6 m \times 6 m \times 20 m with mesh refinement near the injection point. The mesh coarseness is a balance between accuracy and computing time/output file size. Two-way coupling with poroelasticity equations results in computational times much longer than fluid-flow simulation only (Prevost, 2013). Each coupled simulation takes about 64 CPU hours. The lateral extension is sufficiently large to avoid any mechanical boundary effects. The injection zone (IZ) is 100 m thick located at 3,040 m of depth. The injection zone is fully overlain by a 100 m-thick caprock. The low-permeability caprock overlying the injection zone assures CO₂ containment. The five layers

for pressure monitoring are above the caprock and are separated by shales with a thickness of 120 m. We name these layers AIZ 1 to AIZ 5 (above-injection-zone). Each AIZ layer has a thickness of 60 m. The IZ and AIZs have high permeability (300 mD) and are delimited by confining layers with low permeability (100 nD). The storage complex geometry is inspired on shale-sand sequences in young sedimentary basins, such as those in the Gulf of Mexico coast (Beckham, 2018).

The boundaries of the IZ and the AIZ monitoring layers (the edge of this storage complex) are set to constant pressure. The top surface is free to move to capture surface heave due to strains induced in the injection zone and overburden. Only vertical displacement is allowed for the lateral surfaces in the storage complex. We simulate CO₂ injection at the reservoir center with a constant injection rate of 1,008 tons of CO₂ per day (about 0.37 Mt/year). The injector is modeled as a source term in the IZ with an equivalent radius of 0.1 m. The injection operation lasts for two years followed by one year of shut-in. The yellow dots “along the injector” in Fig. 2 represent the hypothetical location of pressure sensors vertically above the injection block, although the physical presence of the injector is not modeled.

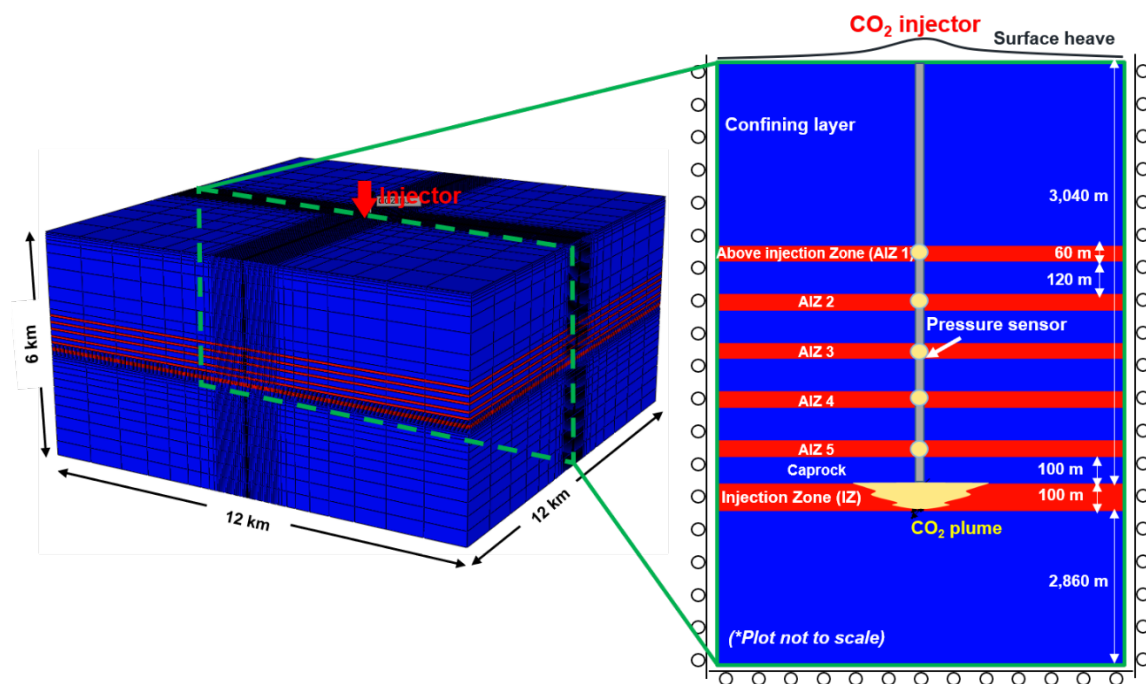


Fig. 2. Reservoir geometry and boundary conditions. CO₂ is injected into the injection zone (IZ) at the depth of 3,040 m. The injection zone is fully overlain by a 100-m low-permeability caprock followed by five above-injection-zone (AIZ) pressure monitoring layers - all above the caprock.

The capillary pressure and relative permeability properties for sand and shale are available in the Appendix 1. We assume isothermal conditions. The viscosity, mass density, compressibility, and mutual solubilities of CO₂ and brine are calculated by the compositional module of CMG-GEM with the corresponding calibrated equations of state; further details are available elsewhere (Jung et al., 2020; Singh & Wheeler, 2016). The poroelasticity equations are extended to two phases within the geomechanical module (Tran et al., 2004). We report liquid pressure (water) in all figures. The capillary pressure is neglected in effective stress poroelastic equations in CMG-GEM. This is a reasonable approximation for IZ and AIZ layers, since the capillary pressure is <1% of the in-situ stress. Notice that the partially undrained loading is only relevant above the caprock in brine-filled layers, so single-phase Eq. 2 still applies with $K_f = K_{brine}$. Other input parameters are listed in Table 1. The assigned values aim at simulating an ideal scenario of sand-shale sequences in the Gulf of Mexico Coast (Jung et al., 2018; Zheng & Espinoza, 2021). A validation of the reservoir simulation model and adopted solution mesh/time step is available in Appendix 2.

The motivation for building a simplified model is to directly observe and characterize pressure variations due to partially undrained loading induced by injection in a simple yet representative model. First, we show the results of an ideal caprock fully extending over the entire injection zone so pressure changes due to undrained loading can be isolated (Section 3). Then, we include possible high permeability paths to differentiate increases of pore pressure caused solely by partially undrained loading from fast hydraulic communication across the caprock (Section 4). The ideal settings serve to capture key features of pressure changes and offer possible interpretations for tracking CO₂ plume and monitoring subsurface leakages. A brief discussion for field cases is available in Section 5.

198

Table 1. Input parameters.

Property	Symbol	IZ/AIZ (sand)	Caprock (shale)
Initial porosity [-]	ϕ	0.22	0.10
Permeability [mD]	k	300	0.0001
Young's modulus [GPa]	E	5	20
Poisson's ratio [-]	ν	0.2	0.3
Bulk modulus* [GPa]	K	2.78	16.67
Biot coefficient** [-]	α	0.92	0.54
Bulk modulus of brine [GPa]	K_f		2.2
Bulk modulus of rock matrix [GPa]	K_m		36

199

Notes: (*) $K = E/[3(1-2\nu)]$, (**) $\alpha = 1 - K/K_m$ 200

3. Results

201

3.1. Pressure increases above a fully covering caprock

202 Numerical simulations show that pressure buildup from CO₂ injection in the IZ causes pore pressure
 203 changes in the storage complex, even outside the IZ, with a low permeability caprock that covers the
 204 entire injection zone (Fig. 3). The changes outside the reservoir are a result of partially undrained
 205 loading and, therefore, depend on space and time. For example, the affected region with $\Delta P > 1$ kPa
 206 extends to as far as 2 km away from the injector at $t = 365$ days. The snapshots of pore pressure
 207 change at various times demonstrate that the five AIZ permeable layers above the caprock respond
 208 to CO₂ injection in the IZ.

209 The pore pressure in overlying shales also changes. The difference between pore-pressure changes
 210 in sand (AIZ monitoring layers) and shale (caprock and other confining layers) is the result of their
 211 distinct mechanical and hydraulic properties including bulk modulus and permeability. The sand,
 212 with a lower bulk modulus, experiences a larger volumetric strain and thus a higher increase of
 213 pressure than the shale (Eq. 3). The sand drains more quickly (less than 10 days in this simulation)
 214 than the shale because of its larger hydraulic diffusivity (Eq. 4 and Fig. 3). As a result, the pressure
 215 increase due to partially undrained loading in sand presents a short-term response (~ 10 days), while
 216 the pressure increase in shale can persist for a relatively long time (> 100 days) after injection starts.

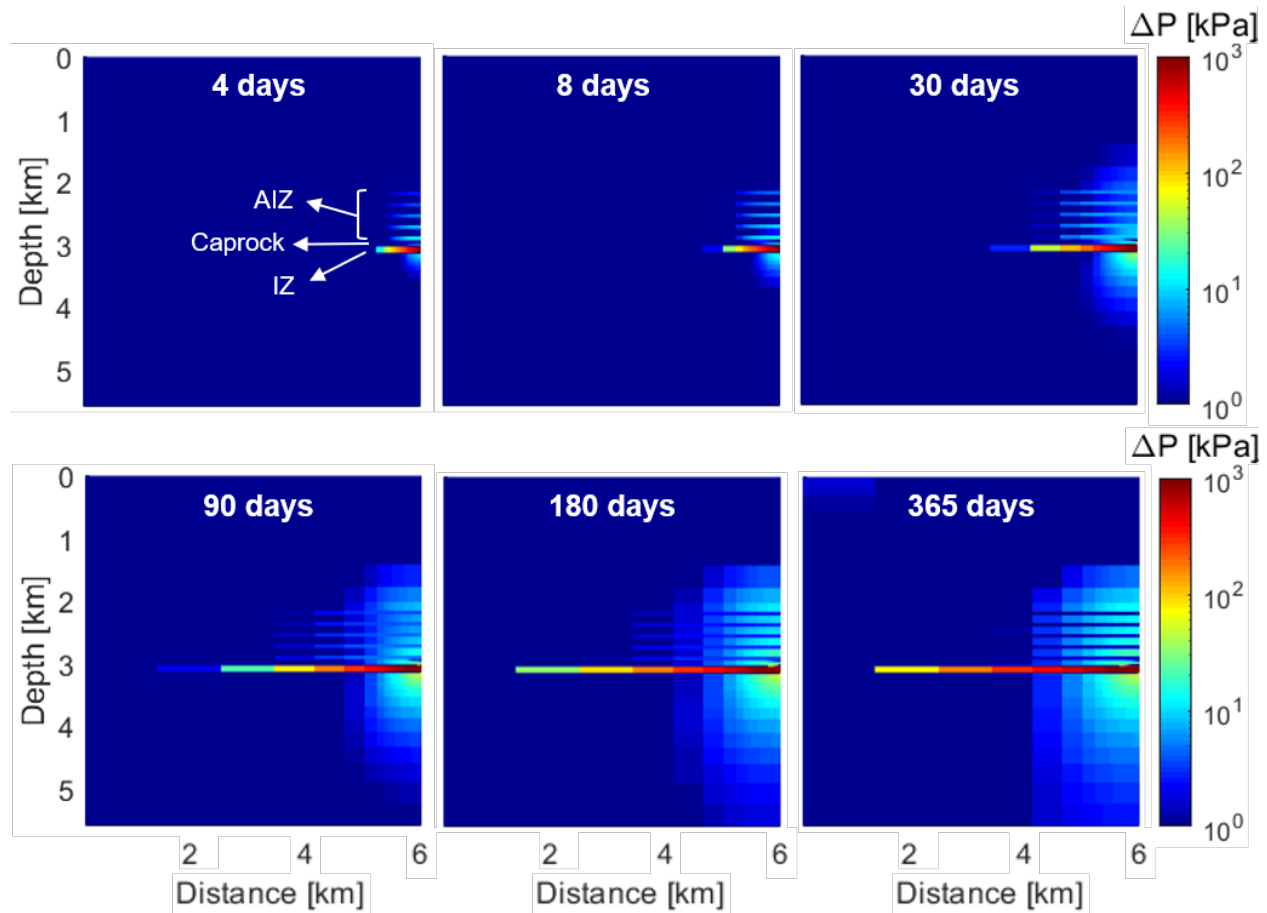


Fig. 3. Pore pressure changes in the CO₂ storage complex (half-domain cross-section shown because of symmetry: injector located on the right boundary). CO₂ injection increases pressure in the injection zone $\Delta P > 1,000$ kPa. Partially undrained loading induced by CO₂ injection causes changes of pore pressure $\Delta P < 20$ kPa outside the reservoir layer. Pore pressure in AIZ sand layers above the fully covering caprock increases in the first 10 days to a peak value and then decreases with time. Pore pressure in shale exhibits more gradual and long-lasting changes than in sands.

The temporal evolution of the injection rate, IZ pressure change ΔP , and AIZ pressure change ΔP during two years of injection and one year of shut-in are closely interrelated (Fig. 4). The IZ pressure increases as much as 1,600 kPa and is followed by a gradual reduction until equilibrium to quasi-steady-state conditions while injection lasts. Instead, the pore pressure in the AIZ (along the injector and above the caprock) exhibits a transient response. The AIZ pressure increases in the first 10 days

and then decreases due to pressure dissipation despite continued injection. The pressure increase in the five AIZ layers above the caprock is less than 5 kPa after 100 days of injection. For example, AIZ 5 (100 m above the IZ) exhibits an instantaneous response to CO₂ injection and fast pressure buildup during the initial stage of injection. A gentle decrease of pressure with time follows after reaching a peak (15 kPa) at $t = 4$ days. The pressure in other distant AIZ layers exhibits a similar trend but with a smaller amount of pressure variations and a delay in reaching the peak which increases with the distance to the injector. Hence, AIZ pressure changes are time/location-dependent and monitoring should focus on the initial stage of injection activities or during periods of changes of injection rate.

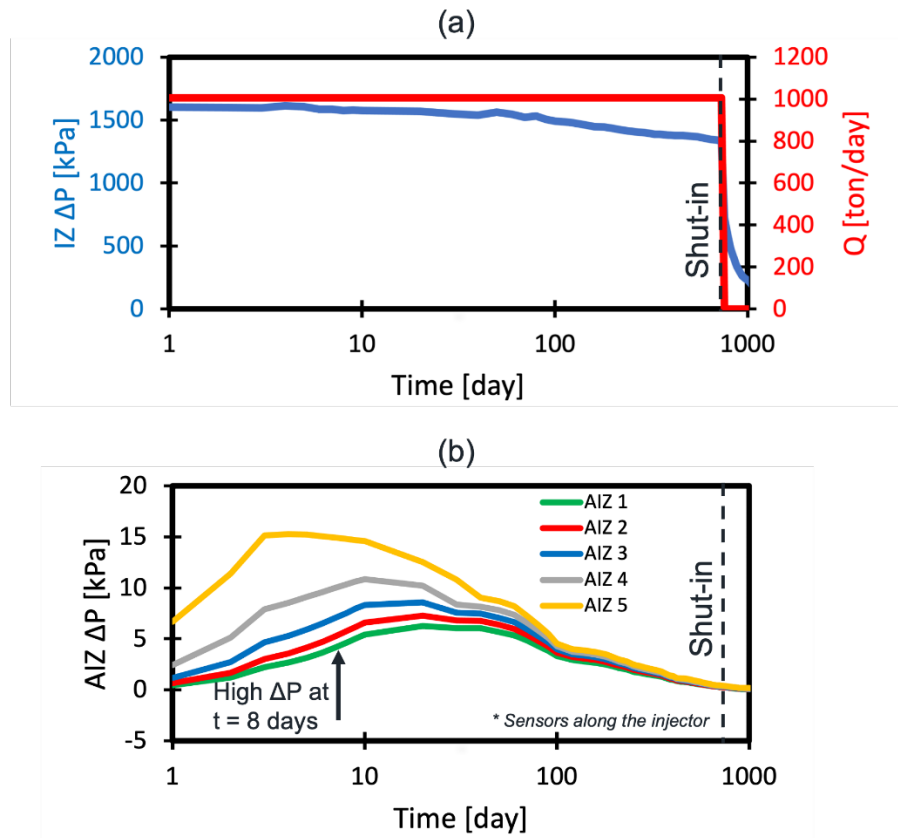


Fig. 4. CO₂ injection rate and pore pressure evolution with a fully covering caprock: (a) injection rate and bottom-hole pressure increase in the injection zone (IZ); (b) pressure increase above the caprock due to partially undrained loading in AIZ monitoring layers.

Fig. 5 shows pressure change and vertical displacement around the injector at $t = 8$ days (when the maximum AIZ ΔP occurs). The AIZ ΔP is larger than 15 kPa within ~ 160 m of the injection point (the distance here refers to the radial distance to the injection point). A strong ΔP signal favors an easy and reliable interpretation of pressure monitoring above the caprock. The AIZ ΔP decreases more quickly with increasing distance from the injector. The AIZ ΔP is less than 4 kPa when the distance is larger than 880 m. The detection limit to pressure variations depends on: (1) pressure transducer resolution, usually about $(\text{maximum pressure}) \times 10^{-6}$ (Santos & Silva, 2022), and (2) background electrical and mechanical noise. For example, the maximum pressure resolution possible for a transducer with 10^{-6} resolution rated to 100 MPa is ~ 0.1 kPa. However, other physical factors and analog to digital conversion may reduce the transducer detection limits. An analog to digital conversion at 16-bit results in a resolution of $(\text{maximum pressure}) / (2^{16}) \sim (\text{maximum pressure}) \times 10^{-5}$, i.e. 1 kPa for a 100 MPa pressure transducer. The typical amplitude of background noise in standard subsurface pressure sensors is around 4 kPa (S. Hosseini et al., 2018; Wiese et al., 2013). Noise is the result of several natural and artificial phenomena such as changes in atmospheric pressure, ocean tides, surface precipitation, and pressure variations associated with measurement instruments and equipment operation. In our generic simulated case, 4 kPa-resolution pressure sensors could detect a pressure change larger than the background noise due to partially undrained loading only if installed closer than ~ 880 m from the injection point. Higher precision pressure transducers and signal analysis could increase the range of reliable pressure monitoring.

The vertical displacement induced by CO_2 injection is the highest closer to the injector (~ 6 mm at the caprock/reservoir interface), which is a result of the reduced effective vertical stress in the IZ. The uplift is higher than 5 mm at less than 160 m from the injection point. Fig. 5 highlights the potential of poroelastic monitoring when ground surface heave (~ 0.3 mm straight above injector in this case) is challenging or impossible to measure on the surface.

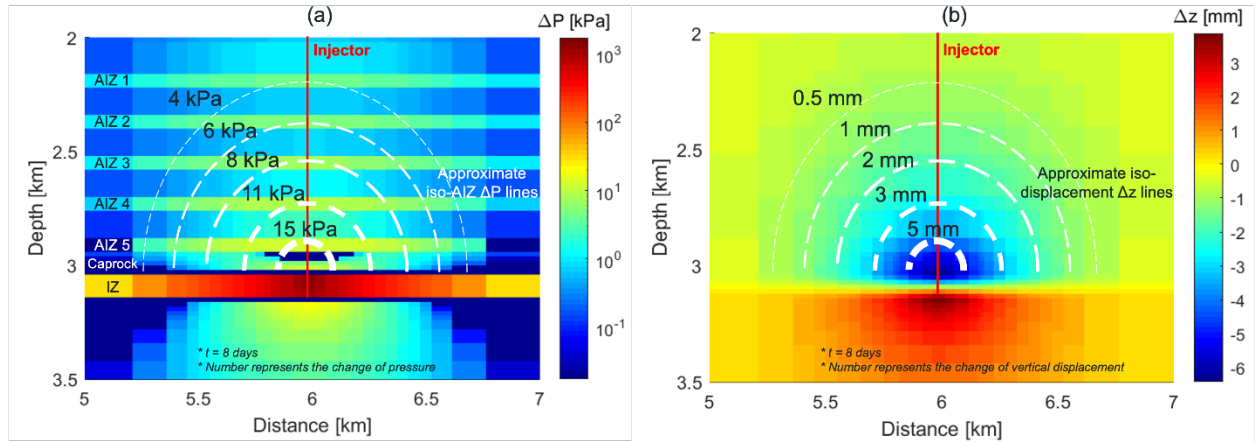


Fig. 5. Poroelastic response at $t = 8$ days due to CO_2 injection with a fully covering caprock: (a) pore pressure changes in the storage complex and pressure fronts around the injector – notice the logarithmic scale; (b) vertical displacement. Surface heave is negligible while pore pressure changes in permeable AIZ formations above the caprock is in the order of $\sim 10^{+1}$ kPa (iso- ΔP lines applicable to AIZ layers only).

3.2. Relationship between pressure changes above the caprock and within the reservoir

The relationship between AIZ ΔP (monitoring layers above the caprock) and IZ ΔP enables the estimation of the IZ pressure from measurements of pressure increases above the caprock. Let us examine the ratio between AIZ ΔP and IZ ΔP along the injector and plot the results as a function of time for the five AIZ permeable layers above the caprock (Fig. 6a). The ratio between AIZ ΔP and IZ ΔP reaches a peak (0.40%, 0.46%, 0.54%, 0.69%, and 0.95%) between 4 to 20 days and then decreases with time. Thus, the pressure increase above the caprock can be as large as $\sim 1\%$ of the IZ pressure increase for this selected reservoir model with a fully covering caprock and the assumed injection schedule.

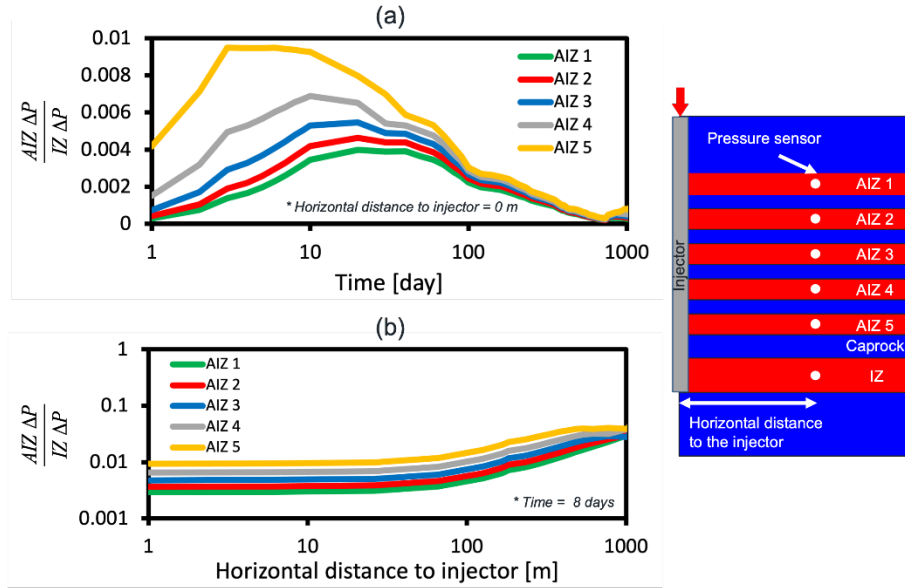


Fig. 6. Relationship between pressure above the caprock AIZ ΔP and IZ ΔP after 8 days: (1) ratio between AIZ ΔP and IZ ΔP as a function of time (sampled points along the injector); (2) ratio between AIZ ΔP and IZ ΔP as a function of horizontal distance to the injector. The maximum ratio is about 1% in the areas of interest.

Fig. 6b shows the ratio $AIZ \Delta P / IZ \Delta P$ for pairs located at the same horizontal distance from the injector at $t = 8$ days. The ratio $AIZ \Delta P / IZ \Delta P$ is nearly constant within 100 m around the injector, which indicates that this ratio does not rely much on the horizontal distance to the injector for five AIZ monitoring layers. For a distance larger than 1000 m, the ratio between AIZ ΔP and IZ ΔP is meaningless since the pressure variations in IZ and AIZ tend to be negligible.

3.3. Interpretation of $AIZ \Delta P / IZ \Delta P$ ratio for plume migration

Fig. 6 demonstrates that the $AIZ \Delta P / IZ \Delta P$ depends mainly on time (after injection) rather than horizontal distance to the injector (particularly when the horizontal distance is less than 100 m). Hence, variations of $AIZ \Delta P / IZ \Delta P$ ratio can tell the evolution of the pressure front with time. Furthermore, the IZ pressure front is related to the saturation front (Fig. 7). Near the injector, the ratio $AIZ \Delta P / IZ \Delta P$ is expected to increase, reach a maximum value, and decrease as a result of CO_2 injection at constant rate (Fig. 6a). The increase of $AIZ \Delta P / IZ \Delta P$ is caused by the pressurization of

the injection zone. The maximum AIZ ΔP /IZ ΔP depends mostly on the imposed rock deformation and poroelastic properties (Eq. 3). The time for the maximum ratio AIZ ΔP /IZ ΔP occurs between 4 and 20 days in our model (Fig. 6a). The CO₂ plume is ~40 m away from the injector at the peak in AIZ 5 (4 days) and 96 m away at the peak in AIZ 1 (20 days) (Fig. 7). The AIZ ΔP /IZ ΔP decrease rate depends on the hydraulic diffusivity of the AIZ. Values of AIZ ΔP /IZ ΔP cannot be larger than the peak in the absence of a high permeability path between the IZ and AIZ layers above the caprock. IZ ΔP can be approximated from analytical solutions or reservoir simulations with known bottom-hole pressure – See Appendix 2 (Avci, 1994; Benson & Doughty, 2006).

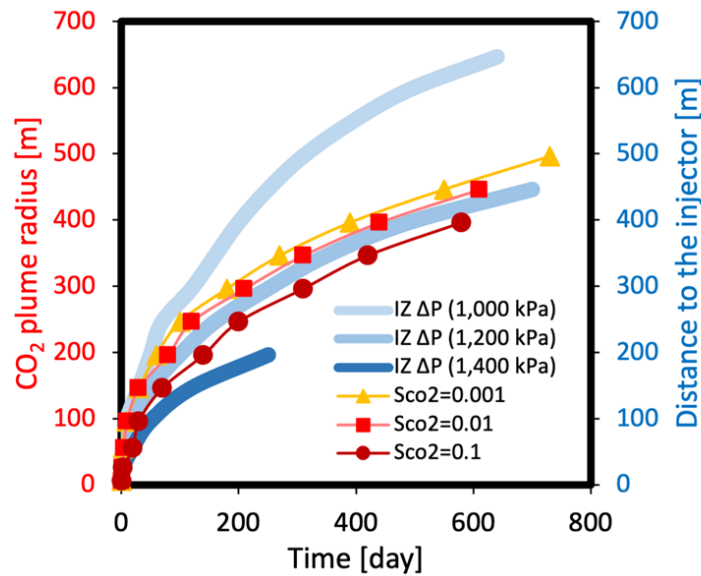


Fig. 7. CO₂ plume radius: the migration of CO₂ plume is tracked through CO₂ saturation. The 1,200 kPa pressure front in the IZ moves simultaneously with the CO₂ plume for a constant injection rate.

4. Discussion: detection of subsurface high permeability paths

4.1. Presence of a high-permeability fault

The previous section highlights that pressure increases above the caprock are possible during CO₂ injection in a reservoir in the absence of any high permeability paths connecting the injection zone and permeable formations above the caprock. The cause is deformation of the rock and relatively fast

compression of the pore fluid. As an extension of our base case with a fully covering low-permeability caprock, let us consider the existence of a fault with high permeability and its influence on the AIZ pore pressure above the caprock. A high permeability fault is set at a distance of 181 m from the injector. The fault intersects all AIZ layers and shales in between spanning over 980 m of vertical length. We model the fault as a wall of grid blocks with a width of 3 m and volume-average permeability equal to 1,000 mD (Childs et al., 2007; Faulkner et al., 2010; Tao et al., 2012; Zheng & Espinoza, 2021b). Fig. 8a compares the pressure increase in five AIZ layers monitored along the injector and the base case.

The pressure increase in AIZ layers above the caprock with a fully covering caprock (base case) is the result of partially undrained loading. However, the AIZ pressure increase in the presence of a high-permeability fault is the result of the combined effects of direct and fast hydraulic communication, and partially undrained loading (Eq. 1). The key features in Fig. 8a include:

- The presence of a high permeability path favors more gradual increases of pore pressure to higher peak values in AIZ layers until injection shut-in (2 years) than the base case (Fig. 6). This additional and sustained pressure increase is the result of fluid communication between the IZ and the AIZ layers above the caprock through the fault.
- The pressure trends in the base and high-permeability fault cases overlap with each other in the first 10 days of CO₂ injection before the effects of partially undrained loading reaches the maximum value. After that, the pressure deviation between the two cases gradually becomes more and more significant. The AIZ ΔP in presence of a high-permeability fault is one order of magnitude larger than the base case after one year of injection. Direct fluid communication, hence, increases AIZ pore pressure ten times more than partially undrained loading after 2 years.

- The pressure buildup due to the hydraulic communication takes time. This is a function of the hydraulic diffusivity of the reservoir rock and high permeability features across the caprock. For example, it takes 26 days for achieving a pressure increase of 100 kPa in AIZ 5 (closest to the injection point) and more than 160 days in the other AIZs for the same pressure increase. Thus, more distant regions exhibit a longer delay in pore pressure increase. The time delay in sensing the pressure increase at different monitoring points helps assess caprock integrity.

Pressure increase larger than expected by sole partially undrained unloading implies fluid transfer (e.g. brine) across the caprock or a sealing fault, but does not necessarily mean a CO₂ leak. Let us also monitor the evolution of CO₂ saturation along the fault. The negligible caprock dip (assumed in this generic model) and buoyancy of bulk CO₂ leads to the rise of CO₂ through the fault and AIZ layers, and thus the pressure in uppermost AIZ 1 is higher than the pressure in other AIZs after two years of CO₂ injection. Here we define the CO₂ arrival at a specific AIZ when CO₂ saturation at the measured point is higher than 0.01. The CO₂ arrival time for five AIZs is 100, 140, 200, 250, 310 days (Fig. 8b). Thus, leakage detection through direct CO₂ saturation monitoring (e.g., through fluid sampling or neutron and resistivity logs) requires at least several months. The AIZ pressure increase occurs much before the change of CO₂ saturation and provides earlier warnings than compositional monitoring at a potential observation well near the fault.

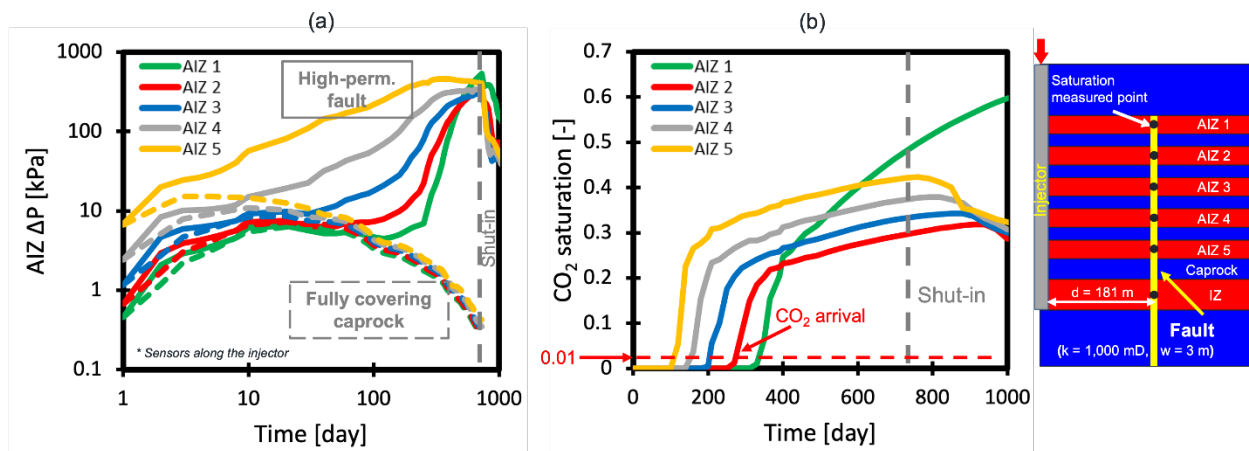


Fig. 8. Time evolution of pore pressure and CO₂ saturation above the caprock in the presence of a high-permeability fault: (a) pressure increase in five AIZ layers along the injector, including the base case with a fully covering caprock and the case with a high-permeability fault; (b) CO₂ saturation in five AIZ layers along the fault. A high-permeability fault results in steady and higher increases of pressure in AIZ layers above the caprock than in the base case.

The CO₂ arrival time can also be approximated with analytical equations (See Appendix 2). For example, for steady-state single phase radial fluid flow the piston-like injection front radius R is a function of time t :

$$R = \sqrt{\frac{Q_{eff}}{\pi h} t} \quad (5)$$

where Q_{eff} is the injection volumetric flow rate and h is the reservoir thickness. CO₂ injection in brine results in poor sweep efficiency, hence the injection rate can be modified to $Q_{eff} = Q/\psi$, where Q is the actual injection rate and ψ is the volume-time average sweep efficiency factor. Typical sweep efficiency factors for CO₂ in oil reservoirs range from 0.20 to 0.28 for 1 pore volume (Lake et al., 2019). Direct comparison of numerical simulations with Eq. 5 results in a reasonable approximation for the CO₂ plume radius as a function of time with $\psi = 0.01$ to 0.015 (Fig. 7). The low value of ψ captures CO₂ high mobility, buoyancy and low solubility in water. Eq. 5 also predicts that CO₂ should arrive to the fault at $R = 181$ m, at $t = 71$ -107 days (with $\psi = 0.01$ to 0.015) in agreement with the CO₂ arrival ($S_{CO_2} = 0.01$) at AIZ 5 at $t \sim 105$ days shown in Fig. 8b.

The pressure distribution shown in Fig. 9 is the result of a high-permeability fault (compare to the base case in Fig. 5a). The high-permeability path releases pressure from the injection zone and exhibits the highest AIZ ΔP in each AIZ. The AIZ ΔP decays with the increase of distance to the high-permeability fault. A rough estimation of the leakage location is possible through pressure monitoring and mapping above the caprock. In this case, the estimated location of the high-permeability path based on the perturbations of pore pressure is about 180 m away from the injector,

which coincides with the actual fault location (the fault location has the highest AIZ ΔP in each monitoring layer). An increase of the number of monitoring wells is expected to provide useful information on the estimation of the extent of subsurface leakages (Zeidouni & Pooladi-Darvish, 2012b). The objective of this paper is to explore the pressure signals above the caprock for different subsurface leakage scenarios through forward modeling (see also next subsections). Though, this simple example could be extended into a formal inverse problem to detect high-permeability pathways with unknown location and arbitrary geometry. Geostatistical data-space approaches and deep-learning algorithms have been used to locate leaks through leaky wellbores considering hydraulic communication only or simplified overburden mechanical models (Sun & Durlofsky, 2019; Tang et al., 2021).

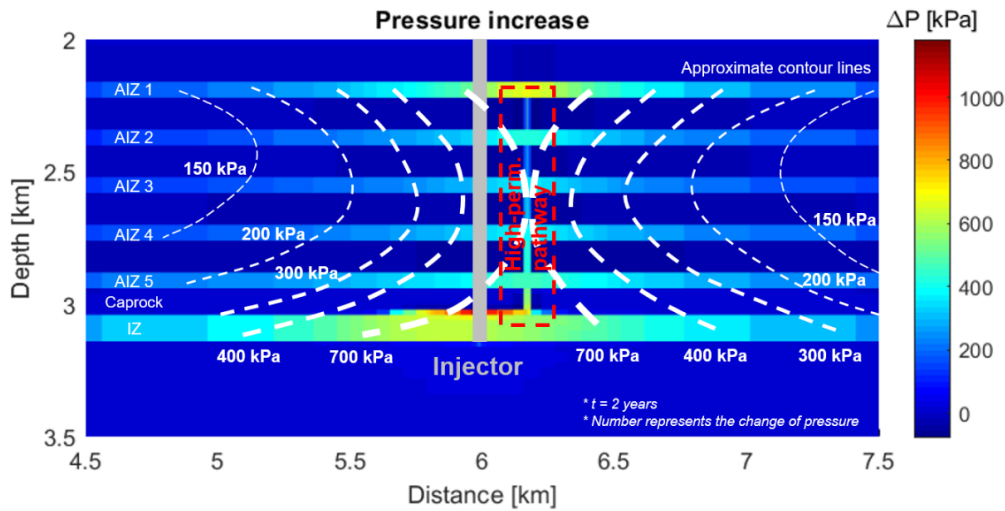


Fig. 9. Pressure change in permeable monitoring layers above the caprock in the presence of a high-permeability fault. The red dashed box highlights the location of the estimated high-permeability path based solely on the observed field pore pressure, which coincides with the location of the high-permeability fault.

4.2. Other relevant scenarios

In this section, we discuss the pressure increases above the caprock in other relevant subsurface scenarios. Fig. 10 presents the distribution of CO_2 plume after two years of injection in six different

cases, including (a) base case with a low-permeability caprock covering all the injection zone, i.e., no fast hydraulic communication or leaks, (b) case with a sealing fault, (c) case with a leaky fault, (d) case with a leaky abandoned well, (e) case with a leaky injector, and (f) case with two injectors. The leaky fault, the sealing fault, the leaky abandoned well, and the second injector are placed at a distance of 181 m from the primary injector. The effective (volume average) permeability of all the leaky grid blocks is 1,000 mD with a thickness of 3 m. The fault permeability has three different values ($k_{fault} = 10, 100, \text{ and } 1,000 \text{ mD}$) in the leaky fault case for a sensitivity test. The second injector starts after 1 year at the same rate of the first injector, up to 1008 ton/day, until the end of the simulation (2 years). Multiple wells are generally used to maximize the available storage space and increase spatial sweep efficiency (Lake et al., 2014; Sun & Durlofsky, 2019). Layer AIZ 1 is overlain by a thick fully covering secondary caprock. The black dots along the primary injector in Fig. 10 represent the location of pressure monitoring sensors.

The CO₂ plume radius is 533 m after 2-years in the base case (cut-off $S_{CO_2}=1\%$ - Fig. 10a). The sealing fault inhibits CO₂ flow on one side and results in preferential CO₂ plume migration opposite to the fault location (Fig. 2b). The presence of leaks reduces the CO₂ plume reach in all leaky cases. High saturation around the leaky well of Fig. 10d in AIZ 5 to 3 is caused by proximity to the injected layer, while high saturation in AIZ 1 is caused by accumulation of CO₂ by buoyancy. AIZ 2 exhibits low saturation because is neither close to the injected layer nor the top layer. Case (d) has been studied previously with focus on pressure time-derivative analysis to discriminate the influence of partially undrained loading from hydraulic communication (Zeidouni & Vilarrasa, 2016). The CO₂ plume reach is the shortest (only 427 m) in the leaky injector case (Fig. 10e).

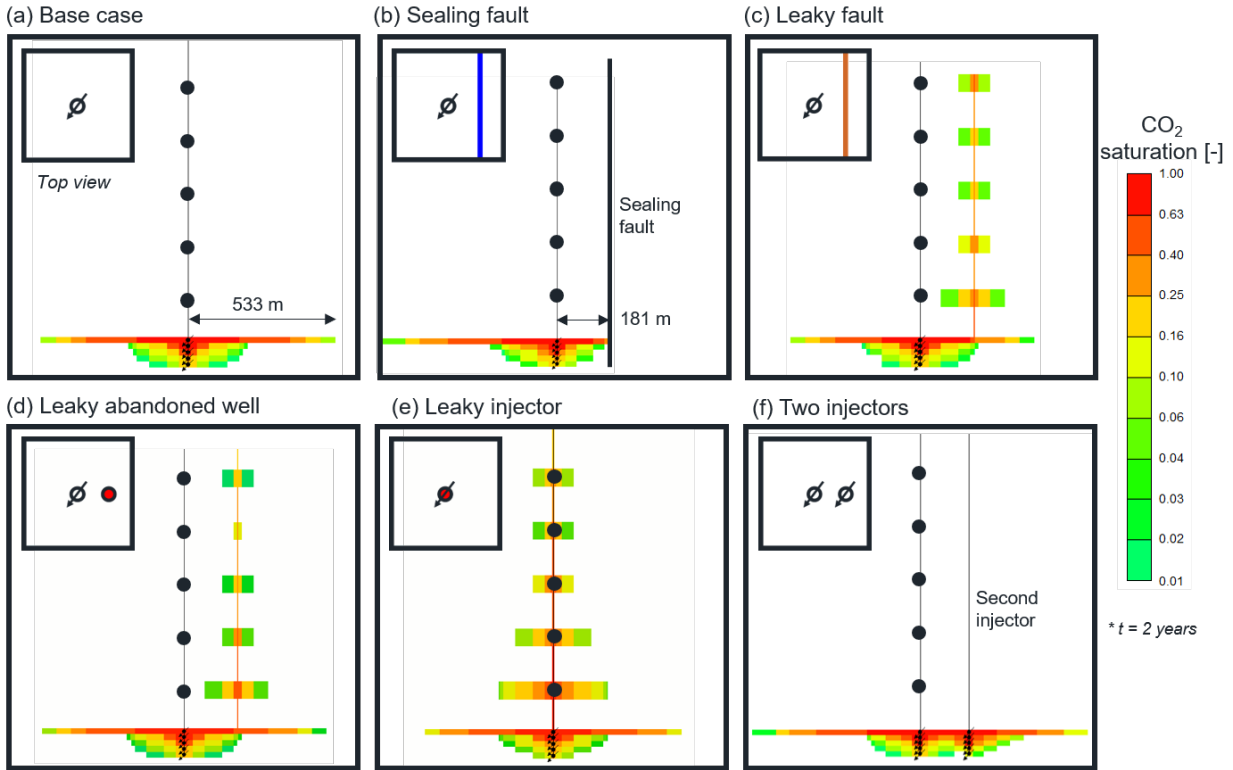


Fig. 10. Distribution of CO₂ plume after two years of CO₂ injection in different scenarios: (a) base case (no leaks through the caprock); (b) case with a sealing fault; (c) case with a leaky fault; (d) case with a leaky abandoned well; (e) case with a leaky injector; and (f) case with two injectors. The inserted plot at the top left of each sub-figure represents the schematic top-view of each layout.

Fig. 11 shows the AIZ pressure increase for the different cases shown in Fig. 10. The presence of high permeability pathways results in the AIZ pressure change in the range of 100 to 1,000 kPa, while pressure increase due to partially undrained loading is characterized by lower values (in the order of magnitude of 10 kPa). All cases with high-permeability pathways lead to eventual CO₂ leaks in our ideal models with no caprock dip. Strong hydraulic communication with no CO₂ leaks could be possible, for example, injecting CO₂ near the top of an anticline with a high-permeability fault downdip not reached by the CO₂ plume.

The leaky injector has the most significant effect on pore pressure changes along the well compared with other leaky scenarios. The leaky abandoned well is 181 m away from the injector and thus

exhibits a delay in pressure increase compared with the leaky injector case. The response for the leaky abandoned-well case overlaps with the response for the base case at the initial stage ($t < 90$ days), suggesting direct fluid flow has not yet arrived at the abandoned well and the primary reason for pressure change is due to partially undrained loading. Afterward, continuous hydraulic communication leads to faster and higher pressure increases.

Variations in fault permeability can result in distinct responses in the AIZ. A permeable fault favors faster fluid communication and higher AIZ pressure increase than the fault with lower permeability. The pressure increase is one order of magnitude smaller for the case with $k_{fault} = 10$ mD than for $k_{fault} = 1,000$ mD. However, if the fault permeability is small enough to inhibit fluid flow (for example, 10 nD), structural sealing will favor a stronger undrained loading above the reservoir and thus higher pressure increase above the caprock (as large as 30 kPa) than the base case with no sealing fault and no leaks.

The addition of the second injector after 1 year results in increases of ΔP by 12 kPa in the first five following days, as a result of partially undrained loading caused by the injection process. The increase of pressure induced by undrained loading follows the principle of superposition (Roussel & Agrawal, 2017), consistently with the assumed linear poroelastic behavior of the rocks. This increase is relatively small compared to changes caused by direct hydraulic communication, yet measurable. Understanding distinct features of pressure increase with or without leaks can help quantify caprock sealing and identify high permeability paths across the caprock.

The transient poroelastic response in the field depends on fluid injection rate and injection schedule. A large injection rate entails fast pressure buildup in the IZ and thus triggers a strong pressure response in the AIZ. For a given injected volume, a step-wise increase of injection rate will mitigate the pore pressure increase from partially undrained loading as increases of volumetric strain happen at the same time pore pressure dissipates in the AIZ. For example, the pressure ramp-up period

should be smaller than ~ 10 days in our base case to induce a noticeable peak and decay of the pressure signal by partially undrained loading in the AIZ monitoring layers.

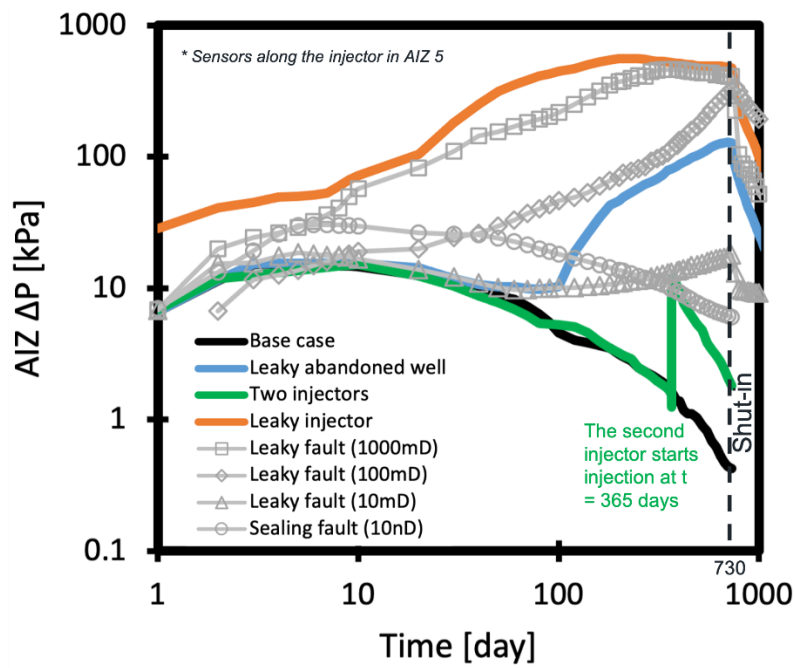


Fig. 11. Pore pressure increases above the caprock for different storage scenarios shown in Fig. 10. The fault permeability varies from 10 nD to 1,000 mD. The effective permeability of leaky blocks in other leaky scenarios is 1,000 mD.

Another possible scenario is a highly compartmentalized and relatively small reservoir. No-flow boundary conditions have a direct impact on pressure in the injection zone and therefore in AIZ layers. Typically, pressure gradients within the reservoir are small under compartmentalized conditions and pressure can remain high over long periods of time after injection shut-in. Such pressure response in the IZ would result in a less pronounced yet more enduring pressure increase in the AIZ assuming a fully-covering caprock. The reservoir model used in this paper is sufficiently large so that the difference between constant pressure or no-flow boundary condition (i.e., compartmentalized) is negligible on AIZ ΔP for ~ 1008 ton/day injection rate over 2 years.

5. Comparison of generic simulation results with field data

There are four CO₂ injection field cases published so far that document pressure monitoring above the injection zone: Cranfield (USA), Ketzin (Germany), Otway (Australia), and Decatur (USA) (Bauer et al., 2016; Ennis-King et al., 2017; Kim & Hosseini, 2014; Wiese et al., 2013). The first two involve pressure monitoring above the caprock similar to the generic model simulated in this study. The last two measure pressure above the injection point but within the same injection unit, such that, thin low permeability layers exist between the injection point and the pressure sensors but there is no thick and continuous low-permeability caprock separating the pressure sensors from the injection point. We include these two most recent field cases in the following summary for the sake of completeness and comparison, although our model is meant to be compared with cases that measure pressure above the caprock.

- *Cranfield, United States, 2009-2011* (Kim & Hosseini, 2014; Tao et al., 2012): CO₂ was injected in a sandstone with a three-step rate schedule. Reservoir (IZ) pressure change reached a maximum of ~8.8 MPa after 250 days of injection. Pore pressure changes are available for two monitoring wells in permeable layers above a ~120 m-thick caprock. The pressure signal of wellbore 31F-2 (68 m down-dip) shows an initial increase of 50-150 kPa followed by a steady increase of 100 kPa, totaling AIZ ΔP / IZ ΔP ~ 0.028. The pressure signal of wellbore 31F-3 (132 m down-dip) shows spikes up to 50 kPa which coincide with changes of injection rate and rapid dissipation (5-20 days), totaling AIZ ΔP / IZ ΔP ~ 0.006. Using Fig. 11 as a guide permits concluding the following: (1) the steady and relatively high pressure increase in well 31F-2 indicates that there might have been hydraulic communication through the caprock along this vertical well, and (2) relatively small pressure spikes indicate full caprock sealing along well 31F-3. None of these cases point necessarily to a CO₂ leak, since the wells are downdip the injection well and there is no field evidence of capillary

sealing breakthrough (Espinoza & Santamarina, 2017). Temperature variations along the wells might have also affected pressure readings (Lindeberg, 2011).

- *Ketzin, Germany, 2011-2012* (Wiese et al., 2013): CO₂ was injected in well Ktzi 201 for over 8 months with a prescribed constant rate interrupted sporadically. Reservoir IZ bottom-hole pressure increased ~0.5 MPa. Monitoring well P300 measured pressure 215 m above injection zone and 120 m updip in the first permeable layer above the caprock. AIZ monitoring showed steady pressure increase reaching a maximum of 7.5 kPa, i.e., AIZ ΔP / IZ ΔP ~ 0.015. The original paper does not offer conclusive proofs for the steady rise in pressure above the caprock and does not discard the possibility of strong hydraulic communication. In fact, there are faults ~2 km away from the injector and monitoring wells behind a dome. A cursory comparison with Fig. 11 indicates hydraulic communication likely through the faults since the monitoring well does not go through the caprock. A CO₂ leak is not a direct implication of hydraulic communication because the injection volume is small and the fault system is mostly behind a dome within the reservoir layer.
- *Decatur, United States, 2011-2014* (Bauer et al., 2016): CO₂ injection was performed at well CCS1 over nearly 3 years at a constant injection rate and close to the bottom of Mt. Simon Formation (sandstone with embedded thin shale layers). As a result, bottomhole pressure at the injector (IZ) changed within ~1 month up to 3.4 MPa at the depth of injection. Additional pressure monitoring above the injection depth but within the Mt. Simon Formation and below the Eau Claire Shale caprock registered steady increases of up to 0.35 MPa in well VW1 within the Mt. Simon Sandstone. This is about 0.10 of the IZ ΔP . The original paper concludes that there is good hydraulic communication between the injection and measured points in agreement with previous expectations and our numerical simulations (Fig. 11). Rapid hydraulic communication is likely due to discontinuities of thin shale layers

within the Mt. Simon Formation, which is capped by the Eau Claire shale and provides further assurance of CO₂ storage.

- *Otway, Australia, 2015-2016* (Ennis-King et al., 2017): CO₂ was injected in the Paarett A Formation with a target injection rate of ~150 tons/day for over 150 days with sporadic shut-ins at the CO₂CRC Otway site in South-West Victoria, Australia. The bottom-hole pressure reached quickly $\Delta P = 0.2$ MPa after injection started or resumed. Pressure monitoring above the injection point exhibited gradual changes of up to 35 kPa well correlated with injection starting/resuming times. This is 0.175 of the pressure at the injection point. This strong hydraulic communication is not surprising since pressure changes are within the same permeable storage unit and under the caprock. In fact, CO₂ plume migration interpreted from time-lapse seismic suggests the presence of a transmissive fault ~300 m away from the injector (Dance et al., 2019).

6. Conclusions

This paper presents numerical simulation results of CO₂ injection and corresponding pore pressure changes above the caprock due to partially undrained loading and hydraulic communication, in views of CO₂ plume tracking and leak monitoring in CO₂ geological storage. The simplified model in this paper serves as an ideal case of pressure monitoring in a sand-shale sequence and aims at providing general trends, although each actual site possesses its own particularities and complexities that may impact those trends. Yet, the results shed light on the general characterization and validation of pressure signals above the caprock as a result of injection-induced poroelastic effects, provide rapid guidelines for analyses of field cases, and serve as validation to build specific models for a given field case geometry, rock properties, and injection schedule. The major conclusions of this paper are:

- Reduced effective stress at the reservoir/storage unit induced by CO₂ injection results in surface heave as well as rock deformation between the injection layer and the ground surface.

A pore pressure variation due to rock deformation and formation fluid compression may appear above the caprock as a result of partially undrained loading.

- The pore pressure increase induced by partially undrained loading above the caprock is non-negligible. The pressure increase is up to 1% of the injection zone (IZ) pressure increase for the chosen storage complex. Pressure increase above the caprock due to partially undrained loading is maximum when rapid changes of pressure occur in the IZ, such as in the initial stage of injection for a constant injection rate schedule, or when injection resumes after a shut-in period. Since the pressure in the injection zone is linked to the migration of the CO₂ plume, it is possible to use pressure changes above the caprock to track the migration of the CO₂ plume in the injection zone.

- High permeability paths across the caprock can increase pressure change above the caprock by one order of magnitude compared to the base case with a fully covering caprock (from ~15 kPa in the base case to 100-1,000 kPa). Such distinctive response is useful to discern pressure changes caused solely by rock compression from pressure changes caused by a high permeability path through the caprock.

- The comparison of generic trends with field cases suggest that: (1) Cranfield monitoring well 31F-3 showed a pressure response above the caprock similar to our simulated base case with no fluid transfer across the caprock, (2) Ketzin monitoring well P300 showed a pressure change above the caprock compatible with fair hydraulic communication between the reservoir and the caprock, and (3) two other cases of monitoring above the injection point within the same injection zone show high hydraulic communication, as expected. A tailored simulation for each case is needed to confirm these cursory interpretations.

- Pressure monitoring above the caprock can be an effective technique to track the extent of the CO₂ plume, quantify hydraulic communication, detect potential leaks, and provide earlier

leak warnings than compositional fluid monitoring. Unexpected pressure increases above the caprock (higher than the range expected for partially undrained loading) are an indication of non-negligible hydraulic communication from the injection zone into overlying formations.

Acknowledgments

The authors are thankful to the Dr. Cécile DeWitt-Morette France-UT Endowed Excellence Fund for making possible this study. We are also grateful to anonymous reviewers who helped us highlight the novelty of this paper and better explain the results.

Appendix 1: Capillary pressure and relative permeability

The capillary pressure in sand is converted from J-functions measured with an air-mercury system to a CO₂-brine system. The relative permeability curve in sand is calculated through the Brooks-Corey drainage model (Jung et al., 2018) (Fig. A1a and Fig. A1b). The capillary pressure and the relative permeability for shale are adapted from the literature and shown in Fig. A1c and Fig. A1d (Bennion & Bachu, 2008; Ren et al., 2016).

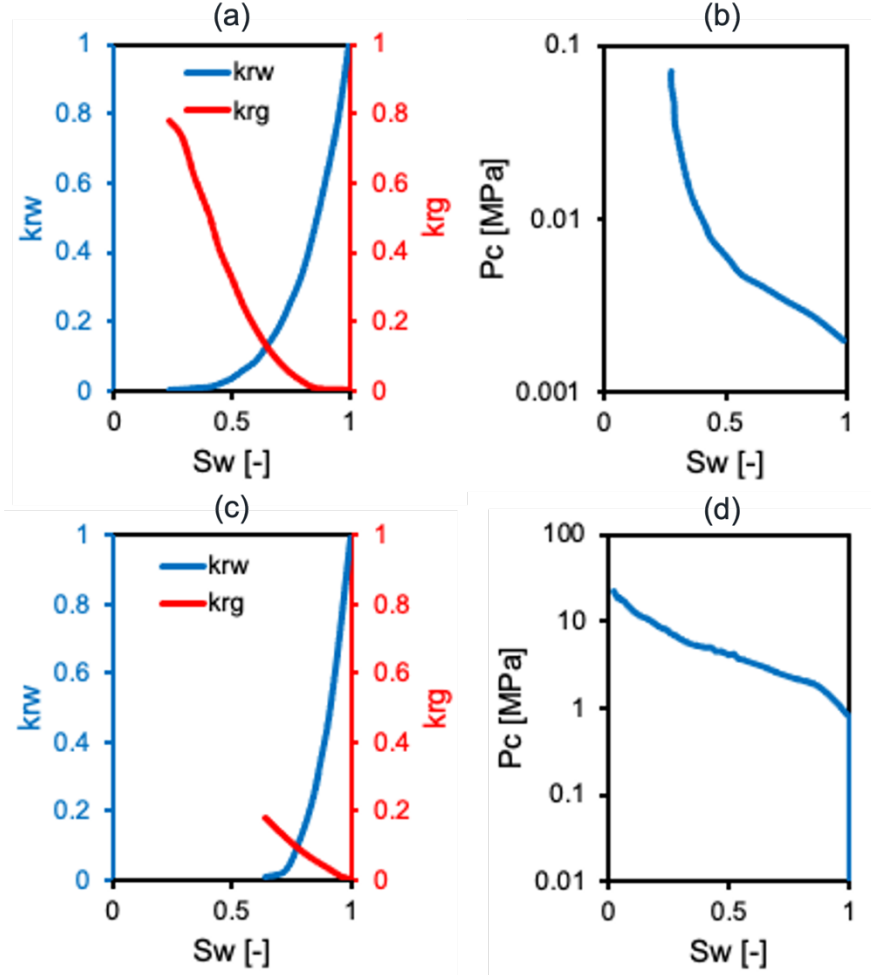


Fig. A1. Capillary pressure and relative permeability in the model: sand (a) and (b); shale (c) and (d).

Appendix 2: Model validation

We validated our numerical model against an analytical solution which combines mass balance for radial flow and multiphase Darcy's law (Benson & Doughty, 2006; Tsopela et al., 2022). The increase of pressure ΔP in the injection zone (IZ) as a function of distance to the injector and time is

$$\Delta P = \frac{Q\mu_{brine}}{4\pi kh} W + \frac{Q\mu_{CO_2}}{2\pi kh} \left(\ln \frac{r_f}{r_w} + \left(\frac{f_{CO_2}}{k_{r_{CO_2}}} \right)_{r_f} - 1 \right) \left(1 - \frac{r_w}{r_f} \ln \frac{r_f}{r_w} \right)$$

where

$$W = -0.5772 - \ln(u_f)$$

$$u_f = \frac{\phi \mu_{brine} C_t r_f^2}{4kt}$$

$$r_f = \left(\frac{Qt}{\pi h \phi S_{CO_2}} \right)^{1/2}$$

Here Q is the injection rate (m^3/s), t is the injection time (s), μ_{CO_2} is the CO_2 viscosity ($Pa \cdot s$), μ_{brine} is the brine viscosity ($Pa \cdot s$), k is the injection zone permeability (m^2), h is the injection zone thickness (m), ϕ is the injection zone porosity, C_t is the injection zone compressibility ($1/Pa$), r_w is the distance to the injector (m). At the CO_2 front, r_f is the radius of the CO_2 front (m) and S_{CO_2} is the average CO_2 saturation at the CO_2 front, which is indicated in Fig. 7a. f_{CO_2} is the CO_2 fractional flow at the CO_2 front, which is obtained through the Buckley-Leverett equation (Peters, 2012). k_{rCO_2} is the CO_2 relative permeability at the CO_2 front, which is calculated through the Corey-type equation as $k_{rCO_2} = k_{rCO_2}^0 \left(\frac{S_{CO_2}}{1-S_{rb}} \right)^n$ (Burton et al., 2009), where S_{rb} is the irreducible brine saturation and $k_{rCO_2}^0$ is the CO_2 relative permeability at the irreducible brine saturation. The capillary pressure and the relative permeability information can be found in Fig. A1. Fig. A2 shows the IZ pressure increase obtained by the numerical model and mesh adopted in this paper compares well to the analytical solution.

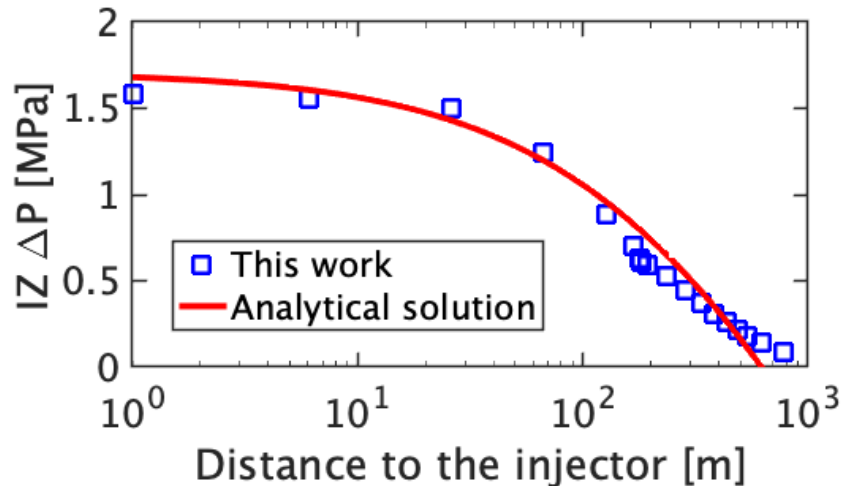


Fig. A2. Comparison of the numerical and the analytical solutions for pressure increase in the AIZ at time = 8 days.

References

- Ajo-Franklin, J. B., Peterson, J., Doetsch, J., & Daley, T. M. (2013). High-resolution characterization of a CO₂ plume using crosswell seismic tomography: Cranfield, MS, USA. *International Journal of Greenhouse Gas Control*, 18, 497–509. <https://doi.org/10.1016/j.ijggc.2012.12.018>
- Arts, R., Eiken, O., Chadwick, A., Zweigel, P., van der Meer, L., & Zinszner, B. (2004). Monitoring of CO₂ injected at Sleipner using time-lapse seismic data. *Energy*, 29(9), 1383–1392. <https://doi.org/10.1016/j.energy.2004.03.072>
- Avci, C. B. (1994). Evaluation of flow leakage through abandoned wells and boreholes. *Water Resources Research; (United States)*, 30:9. <https://doi.org/10.1029/94WR00952>
- Bauer, R. A., Carney, M., & Finley, R. J. (2016). Overview of microseismic response to CO₂ injection into the Mt. Simon saline reservoir at the Illinois Basin-Decatur Project. *International Journal of Greenhouse Gas Control*, 54, 378–388. <https://doi.org/10.1016/j.ijggc.2015.12.015>
- Beckham, E. C. (2018, May). *CO₂ storage in deltaic environments of deposition : integration of 3-dimensional modeling, outcrop analysis, and subsurface application* (Thesis). <https://doi.org/10.15781/T26970G0Z>
- Bennion, B., & Bachu, S. (2008). Drainage and Imbibition Relative Permeability Relationships for Supercritical CO₂/Brine and H₂S/Brine Systems in Intergranular Sandstone, Carbonate, Shale, and Anhydrite Rocks. *SPE Reservoir Evaluation & Engineering*, 11(03), 487–496. <https://doi.org/10.2118/99326-PA>
- Benson, S., & Doughty, C. (2006). Estimation of field-scale relative permeability from pressure transient tests. *Proceedings, EPA CO₂SC Workshop, Berkeley, CA: Lawrence Berkeley National Laboratory*.

625 Burton, M., Kumar, N., & Bryant, S. L. (2009). CO₂ injectivity into brine aquifers: Why relative
 626 permeability matters as much as absolute permeability. *Energy Procedia*, 1(1), 3091–3098.
 627 <https://doi.org/10.1016/j.egypro.2009.02.089>
 628 Cheng, A. H.-D. (2016). *Poroelasticity*. Springer International Publishing. <https://doi.org/10.1007/978-3->
 629 319-25202-5
 630 Childs, C., Walsh, J. J., Manzocchi, T., Strand, J., Nicol, A., Tomasso, M., et al. (2007). Definition of a fault
 631 permeability predictor from outcrop studies of a faulted turbidite sequence, Taranaki, New
 632 Zealand. *Geological Society, London, Special Publications*, 292(1), 235–258.
 633 <https://doi.org/10.1144/SP292.14>
 634 Cihan, A., Birkholzer, J. T., & Zhou, Q. (2013). Pressure buildup and brine migration during CO₂ storage in
 635 multilayered aquifers. *Ground Water*, 51(2), 252–267. <https://doi.org/10.1111/j.1745->
 636 6584.2012.00972.x
 637 Computer Modeling Group Ltd. (2013). *Compositional & Unconventional Reservoir Simulation*. Calgary.
 638 Coussy, O. (2004). *Poromechanics*. John Wiley & Sons.
 639 Dance, T., LaForce, T., Glubokovskikh, S., Ennis-King, J., & Pevzner, R. (2019). Illuminating the geology:
 640 Post-injection reservoir characterisation of the CO₂CRC Otway site. *International Journal of*
 641 *Greenhouse Gas Control*, 86(C). <https://doi.org/10.1016/j.ijggc.2019.05.004>
 642 Detournay, E., & Cheng, A. H. D. (1993). Fundamentals of poroelasticity, 113–171.
 643 <https://doi.org/10.1016/b978-0-08-040615-2.50011-3>
 644 Detournay, E., & Cheng, A. H.-D. (1988). Poroelastic response of a borehole in a non-hydrostatic stress
 645 field. *International Journal of Rock Mechanics and Mining Sciences & Geomechanics Abstracts*,
 646 25(3), 171–182. [https://doi.org/10.1016/0148-9062\(88\)92299-1](https://doi.org/10.1016/0148-9062(88)92299-1)

647 Ennis-King, J., LaForce, T., Paterson, L., Dance, T., Jenkins, C., & Cinar, Y. (2017). Interpretation of Above
 648 Zone and Storage Zone Pressure Responses to Carbon Dioxide Injection in the 2016 CO2CRC
 649 Field Test. *Energy Procedia*, 114, 5671–5679. <https://doi.org/10.1016/j.egypro.2017.03.1706>
 650 Espinoza, D. N., & Santamarina, J. C. (2017). CO 2 breakthrough—Caprock sealing efficiency and integrity
 651 for carbon geological storage. *International Journal of Greenhouse Gas Control*, 66, 218–229.
 652 <https://doi.org/10.1016/j.ijggc.2017.09.019>
 653 Faulkner, D. R., Jackson, C. A. L., Lunn, R. J., Schlische, R. W., Shipton, Z. K., Wibberley, C. A. J., &
 654 Withjack, M. O. (2010). A review of recent developments concerning the structure, mechanics
 655 and fluid flow properties of fault zones. *Journal of Structural Geology*, 32(11), 1557–1575.
 656 <https://doi.org/10.1016/j.jsg.2010.06.009>
 657 González-Nicolás, A., Baù, D., & Alzraiee, A. (2015). Detection of potential leakage pathways from
 658 geological carbon storage by fluid pressure data assimilation. *Advances in Water Resources*,
 659 86(PB). <https://doi.org/10.1016/j.advwatres.2015.10.006>
 660 Hosseini, S., & Alfi, M. (2016). Time-lapse application of pressure transient analysis for monitoring
 661 compressible fluid leakage. *Greenhouse Gases: Science and Technology*, 6(3), 352–369.
 662 <https://doi.org/10.1002/ghg.1570>
 663 Hosseini, S., Shakiba, M., Sun, A., & Hovorka, S. (2018). In-Zone and Above-Zone Pressure Monitoring
 664 Methods for CO2 Geologic Storage. In *Geological Carbon Storage* (pp. 225–241). American
 665 Geophysical Union (AGU). <https://doi.org/10.1002/9781119118657.ch11>
 666 Hosseini, S. A. (2019). Fault leakage detection and characterization using pressure transient analysis.
 667 *Journal of Petroleum Science and Engineering*, 176, 880–886.
 668 <https://doi.org/10.1016/j.petrol.2019.01.099>

669 Hovorka, Benson, S. M., Doughty, C., Freifeld, B. M., Sakurai, S., Daley, T. M., et al. (2006). Measuring
 670 permanence of CO₂ storage in saline formations: the Frio experiment. *Environmental*
 671 *Geosciences*, 13(2), 105–121. <https://doi.org/10.1306/eg.11210505011>
 672 Jung, H., Singh, G., Espinoza, D. N., & Wheeler, M. F. (2018). Quantification of a maximum injection
 673 volume of CO₂ to avert geomechanical perturbations using a compositional fluid flow reservoir
 674 simulator. *Advances in Water Resources*, 112, 160–169.
 675 <https://doi.org/10.1016/j.advwatres.2017.12.003>
 676 Jung, H., Espinoza, D. N., & Hosseini, S. A. (2020). Wellbore injectivity response to step-rate CO₂
 677 injection: Coupled thermo-poro-elastic analysis in a vertically heterogeneous formation.
 678 *International Journal of Greenhouse Gas Control*, 102, 103156.
 679 <https://doi.org/10.1016/j.ijggc.2020.103156>
 680 Jung, Y., Zhou, Q., & Birkholzer, J. T. (2013). Early detection of brine and CO₂ leakage through
 681 abandoned wells using pressure and surface-deformation monitoring data: Concept and
 682 demonstration. *Advances in Water Resources*, 62, 555–569.
 683 <https://doi.org/10.1016/j.advwatres.2013.06.008>
 684 Kim, S., & Hosseini, S. A. (2014). Above-zone pressure monitoring and geomechanical analyses for a
 685 field-scale CO₂ injection project in Cranfield, MS. *Greenhouse Gases: Science and Technology*,
 686 4(1), 81–98. <https://doi.org/10.1002/ghg.1388>
 687 Kim, S., & Hosseini, S. A. (2015). Hydro-thermo-mechanical analysis during injection of cold fluid into a
 688 geologic formation. *International Journal of Rock Mechanics and Mining Sciences*, 77, 220–236.
 689 <https://doi.org/10.1016/j.ijrmms.2015.04.010>
 690 Lake, L., Lotfollahi, M., & Bryant, S. L. (2019). CO₂ Enhanced Oil Recovery Experience and its Messages
 691 for CO₂ Storage. In *Science of Carbon Storage in Deep Saline Formations* (pp. 11–23). Elsevier.
 692 <https://doi.org/10.1016/B978-0-12-812752-0.00002-2>

693 Lake, LW, Johns, R., Rossen, W., & Pope, G. (2014). *Fundamentals of Enhanced Oil Recovery*. Richardson:
694 Society of Petroleum Engineers. Retrieved from [http://store.spe.org/Fundamentals-of-](http://store.spe.org/Fundamentals-of-Enhanced-Oil-Recovery-P921.aspx)
695 [Enhanced-Oil-Recovery-P921.aspx](http://store.spe.org/Fundamentals-of-Enhanced-Oil-Recovery-P921.aspx)

696 Liebscher, A., Möller, F., Bannach, A., Köhler, S., Wiebach, J., Schmidt-Hattenberger, C., et al. (2013).
697 Injection operation and operational pressure–temperature monitoring at the CO2 storage pilot
698 site Ketzin, Germany—Design, results, recommendations. *International Journal of Greenhouse*
699 *Gas Control*, 15, 163–173. <https://doi.org/10.1016/j.ijggc.2013.02.019>

700 Lindeberg, E. (2011). Modelling pressure and temperature profile in a CO2 injection well. *Energy*
701 *Procedia*, 4, 3935–3941. <https://doi.org/10.1016/j.egypro.2011.02.332>

702 Meckel, T., Hovorka, S., & Kalyanaraman, N. (2008). Continuous pressure monitoring for large volume
703 CO2 injections. *Presented at the 9th International Conference on Greenhouse Gas Control*
704 *Technologies (GHGT-9)*.

705 Mishra, S., Oruganti, Y. D., Gupta, N., Ganesh, P. R., McNeil, C., Bhattacharya, I., & Spitznogle, G. (2014).
706 Modeling CO2 plume migration based on calibration of injection and post-injection pressure
707 response at the AEP Mountaineer Project. *Greenhouse Gases: Science and Technology*, 4(3),
708 331–356. <https://doi.org/10.1002/ghg.1434>

709 Namhata, A., Oladyshkin, S., Dilmore, R. M., Zhang, L., & Nakles, D. V. (2016). Probabilistic Assessment of
710 Above Zone Pressure Predictions at a Geologic Carbon Storage Site. *Scientific Reports*, 6(1),
711 39536. <https://doi.org/10.1038/srep39536>

712 Park, Y.-C., Huh, D.-G., & Park, C.-H. (2012). A pressure-monitoring method to warn CO2 leakage in
713 geological storage sites. *Environmental Earth Sciences*, 67. [https://doi.org/10.1007/s12665-012-](https://doi.org/10.1007/s12665-012-1667-2)
714 [1667-2](https://doi.org/10.1007/s12665-012-1667-2)

715 Peters, E. J. (2012). *Advanced Petrophysics: Geology, porosity, absolute permeability, heterogeneity, and*
716 *geostatistics*. Greenleaf Book Group.

717 Prevost, J. (2013). *One-Way versus Two-Way Coupling in Reservoir-Geomechanical Models*.
718 *Poromechanics V - Proceedings of the 5th Biot Conference on Poromechanics* (p. 526).
719 <https://doi.org/10.1061/9780784412992.061>

720 Ren, W., Li, G., Tian, S., Sheng, M., Yang, R., & Wang, T. (2016). Comparison of Capillary Pressure-
721 Saturation Models for Gas-Water Systems in Shale Gas Reservoirs. Presented at the SPE Asia
722 Pacific Oil & Gas Conference and Exhibition, OnePetro. <https://doi.org/10.2118/182461-MS>

723 Roussel, N. P., & Agrawal, S. (2017). Introduction to Poroelastic Response Monitoring - Quantifying
724 Hydraulic Fracture Geometry and SRV Permeability from Offset-Well Pressure Data. Presented
725 at the SPE/AAPG/SEG Unconventional Resources Technology Conference, Unconventional
726 Resources Technology Conference. <https://doi.org/10.15530/URTEC-2017-2645414>

727 Rutqvist, Vasco, D. W., & Myer, L. (2009). Coupled reservoir-geomechanical analysis of CO₂ injection at
728 In Salah, Algeria. *Energy Procedia*, 1(1), 1847–1854.
729 <https://doi.org/10.1016/j.egypro.2009.01.241>

730 Rutqvist, J., Vasco, D. W., & Myer, L. (2010). Coupled reservoir-geomechanical analysis of CO₂ injection
731 and ground deformations at In Salah, Algeria. *International Journal of Greenhouse Gas Control*,
732 4(2), 225–230. <https://doi.org/10.1016/j.ijggc.2009.10.017>

733 Ryu, J., Espinoza, D. N., Balhoff, M. T., & Tavassoli, S. (2019). Simulation of Fault Reactivation Using the
734 HISS Model. Presented at the SPE Annual Technical Conference and Exhibition, OnePetro.
735 <https://doi.org/10.2118/196153-MS>

736 Santos, E. J. P., & Silva, L. B. M. (2022). High-resolution pressure transducer design and associated
737 circuitry to build a network-ready smart sensor for distributed measurement in oil and gas
738 production wells. *Journal of Petroleum Exploration and Production Technology*.
739 <https://doi.org/10.1007/s13202-021-01422-9>

740 Segall, & Fitzgerald. (1998). A note on induced stress changes in hydrocarbon and geothermal reservoirs.
741 *Tectonophysics*, 289(1–3), 117–128. [https://doi.org/10.1016/S0040-1951\(97\)00311-9](https://doi.org/10.1016/S0040-1951(97)00311-9)

742 Singh, G., & Wheeler, M. F. (2016). Compositional flow modeling using a multi-point flux mixed finite
743 element method. *Computational Geosciences*, 20(3), 421–435. [https://doi.org/10.1007/s10596-](https://doi.org/10.1007/s10596-015-9535-2)
744 015-9535-2

745 Sun, W., & Durlofsky, L. (2019). Data-space approaches for uncertainty quantification of CO₂ plume
746 location in geological carbon storage. *Advances in Water Resources*.
747 <https://doi.org/10.1016/J.ADVWATRES.2018.10.028>

748 Tang, M., Ju, X., & Durlofsky, L. J. (2021). Deep-learning-based coupled flow-geomechanics surrogate
749 model for CO₂ sequestration. Retrieved from <https://arxiv.org/abs/2105.01334v1>

750 Tao, Q., Bryant, S. L., Meckel, T., & Luo, Z. (2012). Wellbore Leakage Model for Above-Zone Monitoring
751 at Cranfield, MS. Presented at the Carbon Management Technology Conference, Carbon
752 Management Technology Conference. <https://doi.org/10.7122/151516-MS>

753 Tran, Settari, A., & Nghiem, L. (2004). New Iterative Coupling Between a Reservoir Simulator and a
754 Geomechanics Module. *SPE Journal*, 9(03), 362–369. <https://doi.org/10.2118/88989-PA>

755 Tran, D., Shrivastava, V. K., Nghiem, L. X., & Kohse, B. F. (2009). Geomechanical Risk Mitigation for CO₂
756 Sequestration in Saline Aquifers. Presented at the SPE Annual Technical Conference and
757 Exhibition, OnePetro. <https://doi.org/10.2118/125167-MS>

758 Tsopela, A., Bere, A., Dutko, M., Kato, J., Niranjana, S. C., Jennette, B. G., et al. (2022). CO₂ injection and
759 storage in porous rocks: coupled geomechanical yielding below failure threshold and
760 permeability evolution. *Petroleum Geoscience*, 28(1). <https://doi.org/10.1144/petgeo2020-124>

761 Wiese, B., Zimmer, M., Nowak, M., Pellizzari, L., & Pilz, P. (2013). Well-based hydraulic and geochemical
762 monitoring of the above zone of the CO₂ reservoir at Ketzin, Germany. *Environmental Earth*
763 *Sciences*, 70(8), 3709–3726. <https://doi.org/10.1007/s12665-013-2744-x>

- Zeidouni, M., & Pooladi-Darvish, M. (2012a). Leakage characterization through above-zone pressure monitoring: 1—Inversion approach. *Journal of Petroleum Science and Engineering*, 98–99, 95–106. <https://doi.org/10.1016/j.petrol.2012.09.006>
- Zeidouni, M., & Pooladi-Darvish, M. (2012b). Leakage characterization through above-zone pressure monitoring: 2—Design considerations with application to CO₂ storage in saline aquifers. *Journal of Petroleum Science and Engineering*, 98–99, 69–82. <https://doi.org/10.1016/j.petrol.2012.09.005>
- Zeidouni, M., & Vilarrasa, V. (2016). Identification of above-zone pressure perturbations caused by leakage from those induced by deformation. *Environmental Earth Sciences*, 75(18), 1271. <https://doi.org/10.1007/s12665-016-6090-7>
- Zhang, L., Dillmore, R., Namhata, A., & Bromhal, G. (2018). Feasibility of CO₂ migration detection using pressure and CO₂ saturation monitoring above an imperfect primary seal of a geologic CO₂ storage formation: a numerical investigation. *Computational Geosciences*, 22(3), 909–923. <https://doi.org/10.1007/s10596-018-9732-x>
- Zhang, L., Wang, Y., Miao, X., Gan, M., & Li, X. (2019). Geochemistry in geologic CO₂ utilization and storage: A brief review. *Advances in Geo-Energy Research*, 3(3), 304–313.
- Zheng, X., & Espinoza, D. N. (2021a). Measurement of Unloading Pore Volume Compressibility of Frio Sand Under Uniaxial Strain Stress Path and Implications on Reservoir Pressure Management. *Rock Mechanics and Rock Engineering*. <https://doi.org/10.1007/s00603-021-02571-3>
- Zheng, X., & Espinoza, D. N. (2021b). Multiphase CO₂-brine transport properties of synthetic fault gouge. *Marine and Petroleum Geology*, 129, 105054. <https://doi.org/10.1016/j.marpetgeo.2021.105054>